Chapter 3

Fabrication and Characterization of ZnO Nanoparticles based Resistor for NO_2, H_2, CO, Ethanol and Propanol Detection

3.1 Introduction

It is required to realize a facile and reliable gas sensor that would be suitable for wide variety of gas detection ranging from hazardous, explosives, pollutants and toxics (Mao, Lu and Chen, 2014). Nitrogen dioxides (NO_2) is one of the pollutants gas that is generally emitted because of incomplete combustion of fuels in automobiles, excessive use of pesticides and insecticides in agriculture (Thu *et al.*, 2017a), aquatic sapling, home heaters, industry, and furnaces etc. In order to monitor and control the concentration of NO_2, it is very important to develop high- performance compact NO_2 sensor, that detect NO_2 swiftly and selectively (Chougule, Sen and Patil, 2012a; Navale *et al.*, 2014; Thu *et al.*, 2017b; Urasinska-Wojcik *et al.*, 2017).

Nano-structured semiconducting metal oxides (SnO_2, WO_3, ZnO etc.) (Sadek *et al.*, 2007; Rai and Yu, 2012; Rai *et al.*, 2012; Shim *et al.*, 2014; Van Quang *et al.*, 2014) based gas sensors have drawn great attention for NO_2 detection since long time due to their advantageous features such as large surface to volume ratio, low cost and facile fabrication (Wang *et al.*, 2006; Chougule, Sen and Patil, 2012a). ZnO is one of the best SMO materials which has used for detection of toxic and explosive gases at relatively low operating temperature. The nanostructure of the ZnO thin film has led to numerous adsorption sites and its large pore size which increase the interaction of gas molecules to the sensor's surface which results in the increase in sensitivity.

This chapter develops the brush coated ZnO nanoparticles based resistor and discusses the fabrication and characterization tools required for ZnO-resistor. The sensor has been tested upon the NO_2, H_2, CO, ethanol and propanol gases and observed sensitivity in terms of percent/ppt (parts per thousand) in the temperature range from 150 to 350 °C. This sensor has been further utilized for exploring NO_2 sensing properties. The obtained results have been explained by the surface and subsurface adsorption of target gas on the ZnO nanoparticles based thick film.

3.2 Resistor Fabrication Tools

The resistor fabrication and characterization facilities available in laboratory have been briefly discussed in this section which is as follows:

3.2.1 Manual Thick Film Printer

The manual thick film printer (model-65; DEK, Germany) is shown in Figure 3.1. This manual printer consists of a substrate holder along with vacuum hold facility in order to avoid any displacement or misalignment of the substrate during screen printing process. Squeegee blade is made of urethane rubber which passes over the screen surface and forces the printing paste (conducting or insulating paste) through well designed pattern on the screen opening.

Figure 3.1: Front view of thick film printer

3.2.2 Electric Oven

Figure 3.2 shows the image of a conventional electric oven (Metzer Biomedical and Electronics Pvt. India Ltd.). It consists of a thermally isolated chamber that is used for drying the film sample immediately after print leveling. This oven consists of a simple thermostat which is used to select the desired temperature (in the rage 100 – 125 °C). It also has a timer which allows the oven to be turned on and off automatically at a pre-set temperature. The oven has a provision to control the temperature precisely from room temperature to 250 °C. Drying of the film is necessary to avoid formation of blisters in the film due to rapid evaporation during firing at a relatively higher temperature.

Figure 3.2: Front view of electric Oven

3.2.3 Conveyor Belt Furnace

The moving belt type Conveyor Belt Furnace (model-840; DEK, Germany) has been shown in Figure 3.3 for firing the thick film. After drying the print at a lower temperature 120 fabrication step is necessary for proper adherence of the film to the substrate/other film. In addition, the film acquires all the desired electric properties after firing. Firing the film with a

standard firing profile (i.e. belt speed, peak firing temperature and firing time in the peak temperature zone) is necessary in order to have a consistency in the response of the device. The furnace has all these provision. The belt itself has a metal chain mesh-type structure that does not deform at very high temperatures within the furnace during firing.

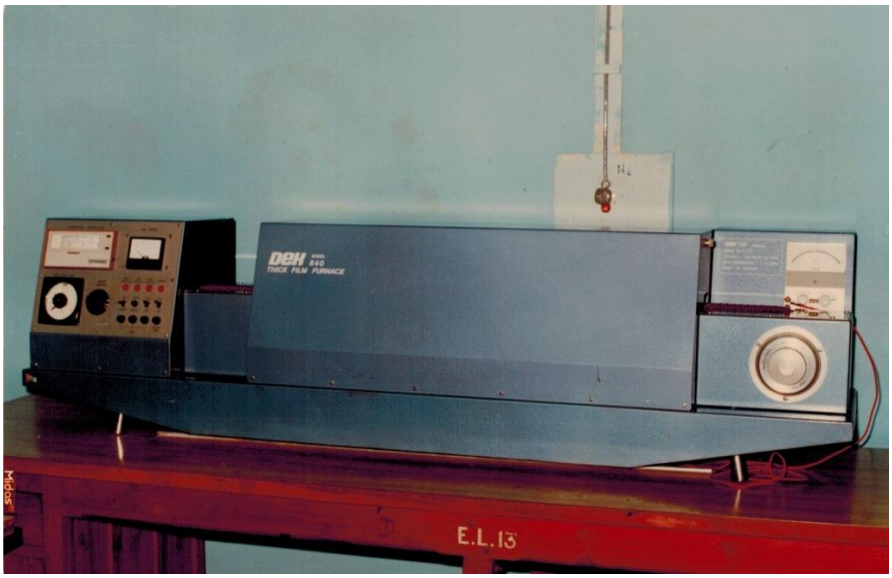

Figure 3.3: Front view of the conveyor belt furnace

3.2.4 Calcination Furnace

The calcinations furnace has been shown in the Figure 3.4. It consists of a general purpose temperature controller ranging from room temperature to 1200 °C. It possesses a muffled glass tube having a diameter of around 2.5 inches for holding the sample. The heating element is helically wounded around the circular glass tube to generate a stable temperature.

Figure 3.4: Front view of a calcination furnace

3.3 Material Characterization Tools

The material characterization is a very important part to analyze sensors characteristic. This section briefly discusses the working principles and different film characterization techniques. The associated instruments for investigating the structural, electrical and surface characteristic of the film are briefly given below:

3.3.1 Field Emission Scanning Electron Microscopy (FESEM)

The electron microscope is used to enlarge the sample surface on a very fine scale. It uses high energy electron beam to create a highly-magnified image. The scanning electron microscope (SEM) is similar to electron microscope that builds images of sample's surface by scanning with high energy electron beam. A field emission SEM (FE-SEM) is a special type of SEM where sample's surface is scanned by a high energy narrow probing beam of the electron. These narrow beams of electrons directly interact with the atoms available at the surface of the sample and produce signals which consist of information about surface morphology and topography (Gnanamoorthy, Karthikeyan and Prabu, 2014). Figure 3.5

depicts the schematic unit of FESEM, in which the electron gun provides a low and stable flow of electron in a small beam that results improvement in spatial resolution and minimize sample charging and damage.

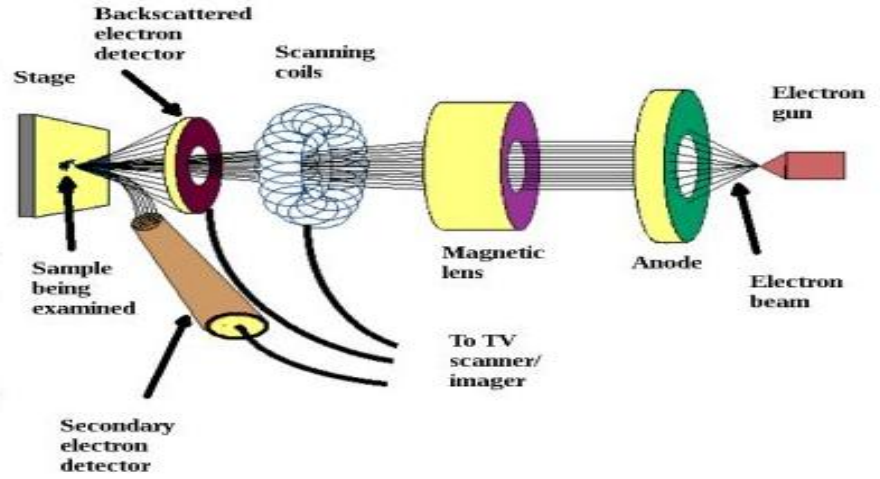

Figure 3.5: Electron beam follows the path through lences (Harrers, 2016)

3.3.2 Energy Dispersive X-ray Spectroscopy (EDS)

Energy dispersive X-ray spectroscopy (EDS) is a micro-analytical technique used along with scanning electron microscopy (SEM). It determines the chemical elements from the X-ray emission that are present in a sample composition. The X-ray is generated through the sample by the high energy electron beam. In the sample, the atoms contain ground state electrons at discrete energy levels which are bounded through their nucleus. When electron beams are incident to the atoms, the electrons in an inner shell are excited to higher level. In order to relaxation, an electron from a higher level down into the lower level and releases extra energy in the form of X-rays. The X-ray energy can be determined by the energy difference between these two energy levels, which is unique for each element. Figure 3.6 shows the working principle of the energy dispersive spectrometer.

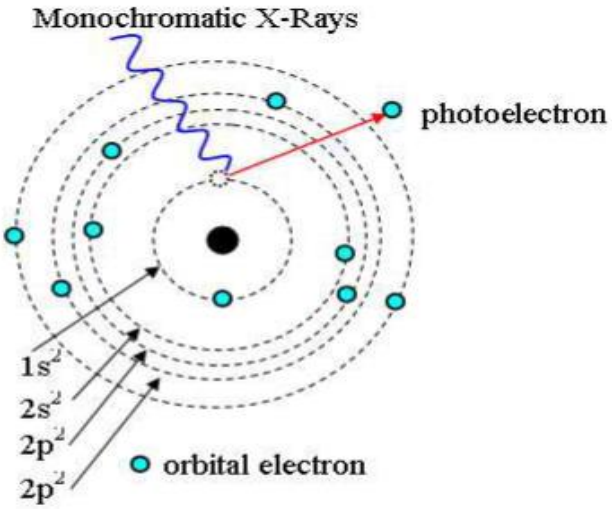

Figure 3.6: X-ray photon being absorbed by an orbital electron (Kamarulzaman and Jaafar, 2003)

3.3.3 X-Ray Diffraction (XRD) Analysis

The X-ray diffraction (XRD) analysis has been used for identifying the crystallographic structure of natural or synthesized materials. It uses diffraction of incidental X-rays into many directions that caused by crystalline atoms as shown in Figure 3.7. The X-ray diffraction mainly focused on X-rays interaction with crystalline atoms which is governed by the Bragg's law (Connolly, 1996).

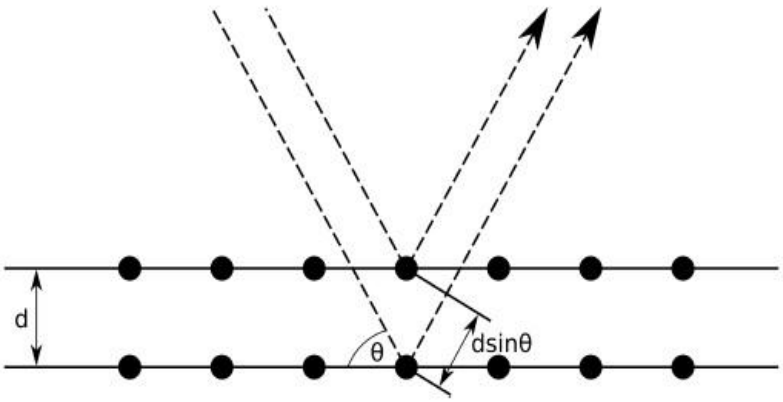

Figure 3.7: A schematic of X-ray diffraction pattern [IR5].

Bragg's law states that when a monochromatic X-ray incident upon the atoms in a crystal lattice, the rays scatters into the various directions. Thus, crystal lattice acts as a series of the parallel plane which reflects the X-rays accordingly. Figure 3.7 shows the schematic of X-ray diffraction where d represents the distance between the parallel plane and θ is the angle in which X-ray impinge to an atom of the plane. The reflected beam shows maximum intensity at angles where the path difference between two reflected waves from two different planes is an integral multiple of the operating wavelength "λ" (Swaminathan, 2013). According to the Bragg's law if there are n number of diffraction occurs at d lattice spacing (Connolly, 1996), the relationship is shown in Equation (3.1)

$$2\mathrm{d}\sin\theta = n\lambda \tag{3.1}$$

The X-ray diffraction reveals the information about the crystal structure, orientation and average crystallite size and stresses the films. The crystalline size of the sample can be calculated from the Debye Scherer's formula by Equation (3.2)

$$D = \frac{K\lambda}{\beta\cos\theta}, \tag{3.2}$$

Where K is a dimensionless shape factor with a value close to unity whereas the shape factor has a typical value of about 0.9 and β is the full width at half maximum intensity in radians.

3.3.4 Atomic Force Microscopy (AFM)

Atomic force microscopy (AFM) is one kind of scanning probe microscopes (SPM) which was invented by Binnig *et al*. (Quate, 1986) in 1986. In an AFM setup, a laser beam is focused onto the back side of a cantilever and reflected to a photodetector as shown in Figure 3.8. When the tip of cantilever moves over the sample surface, the motion is detected by the laser beam reflected on the photodiode detector. The gradual motion of the cantilever

(vertical and lateral) is used as topographic feedback. The cantilever and the sample are thus not necessarily conductive. Typical cantilevers used in AFM are made of silicon or silicon nitride, having a tip radius of a few to tens of nanometers.

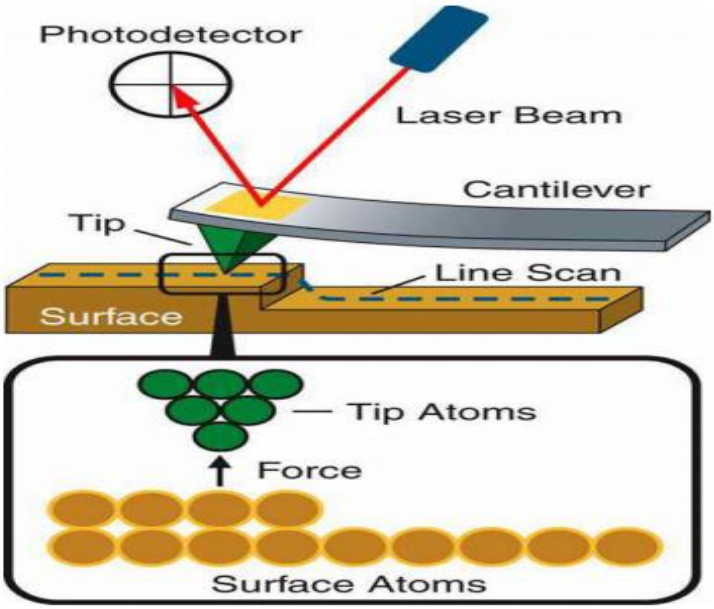

Figure 3.8: A schematic of the AFM set-up (Jena, 2014).

3.4 In-House Developed Measurement Set-up

An innovative approach was used to develop a test chamber for the sensor characterization, wherein the test gas composition could be well controlled. The in-house measurement set-up has been illustrated in Figure 3.9. The set-up comprising of a glass sealed chamber of around 3 liters four probe facility. In this measurement set-up, the electrodes of the sensor are connected to a digital multimeter (195 A; Kethley, USA) in order to measure the resistance of the sensor under test. The heater on the back side of sensor substrate generates the desired temperature by controlling the power dissipated in the heater coil during the course of measurement. The test chamber has a provision for injecting the gases through rubber septum using air tight scaled syringe. Target gases are injected into a

chamber through the inlet valve which is placed at the top of the test chamber. After injecting the gases, the chamber is flushed with clean air by opening the outlet valve. After allowing complete recovery of the sensor, the chamber is ready for another set of observation.

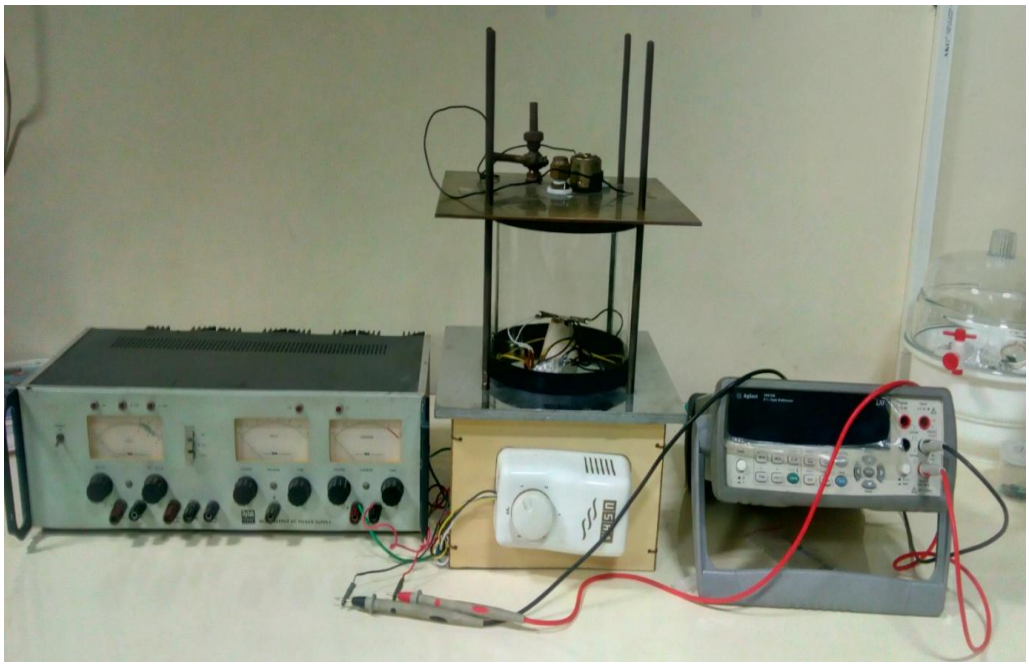

Figure 3.9: Front view of In-house developed a gas-sensing measurement system.

3.5 Experimental Details

The fabrication of resistor is accomplished by depositing a well defined electrode and heater pattern on an insulating substrate. The present work utilized the thick film technology for fabrication of integrated elements (electrode and heater) of bush coated ZnO-resistor. Different fabrication steps which are followed for the fabrication of ZnO resistive sensor has been explained in the flow chart as shown in Figure 3.10.

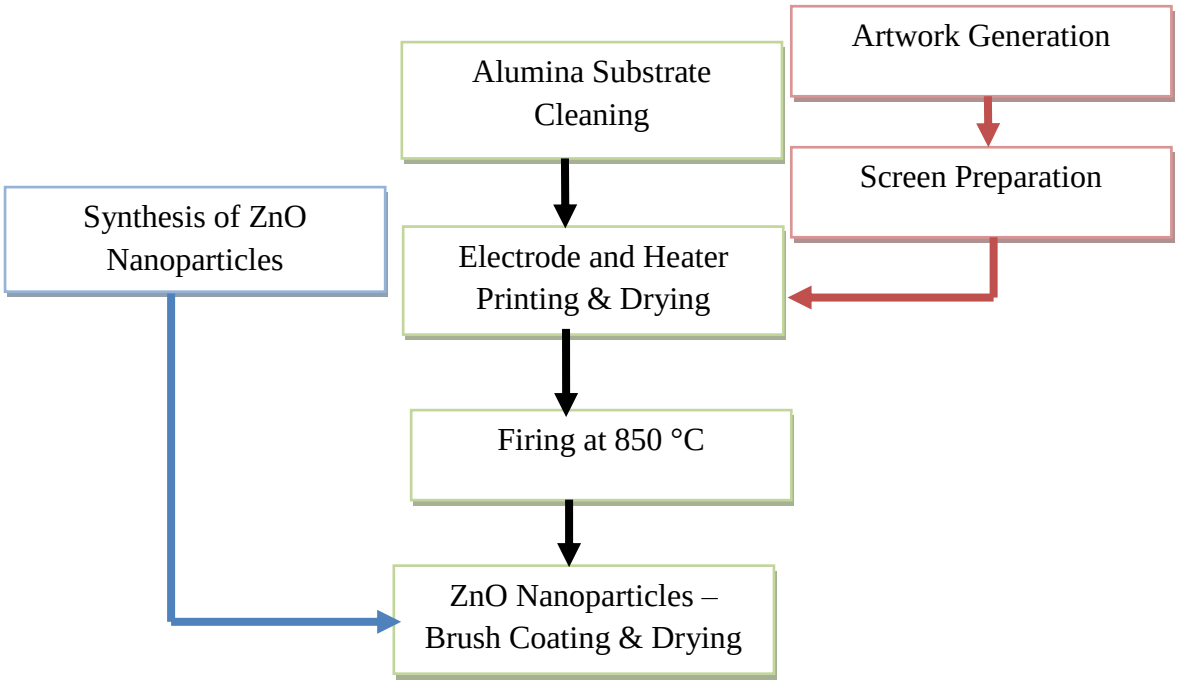

Figure 3.10: The fabrication process flow of ZnO-resistor as a gas sensor.

3.5.1 Synthesis Process of ZnO Nanoparticles

ZnO nanopowder was synthesized using the sol-gel method. To prepare ZnO powder, precursors used were zinc acetate dihydrate [$Zn(CH_3COO)_2 \cdot 2H_2O$] and sodium hydroxide (NaOH). The synthesis process requires two separate solutions. First, 0.1 M solution of $Zn(CH_3COO)_2 \cdot 2H_2O$ was prepared by mixing the ~ 1.09 g of $Zn(CH_3COO)_2 \cdot 2H_2O$ into the 50 ml methanol and was vigorously stirred at 70 °C for 2 h. Second, 0.5 M solution NaOH was prepared by mixing 1 g of NaOH into 50 ml DI water and was stirred 10 min. After that, the NaOH solution added into $Zn(CH_3COO)_2 \cdot 2H_2O$ solution drop by drop and continuously stirred at 70 °C until the pH value of stock solution approaches to 8. This results in a white precipitate. This white precipitate consists of ZnO nanoparticles as well as residue products like Sodium acetate dihydrate ($NaCH_3OOH$) and H_2O. Further, the precipitate was kept for 4 h. at 120 °C. The complete chemical reaction results in ZnO nanoparticle which can be represented by the following chemical Equation (3.3) (Bari *et al.*, 2009; Hasnidawani *et al.*, 2016)

$$Zn\ (CH_3COO)_2 + 2NaOH \rightarrow ZnO + 2\ NaCH_3COO + H_2O \quad (3.3)$$

The resultant products were further calcinated at 600 °C for 2 hours to obtain the ZnO NPs in powder form. The flowchart for the preparation of ZnO nanoparticle powder is given in Figure 3.11.

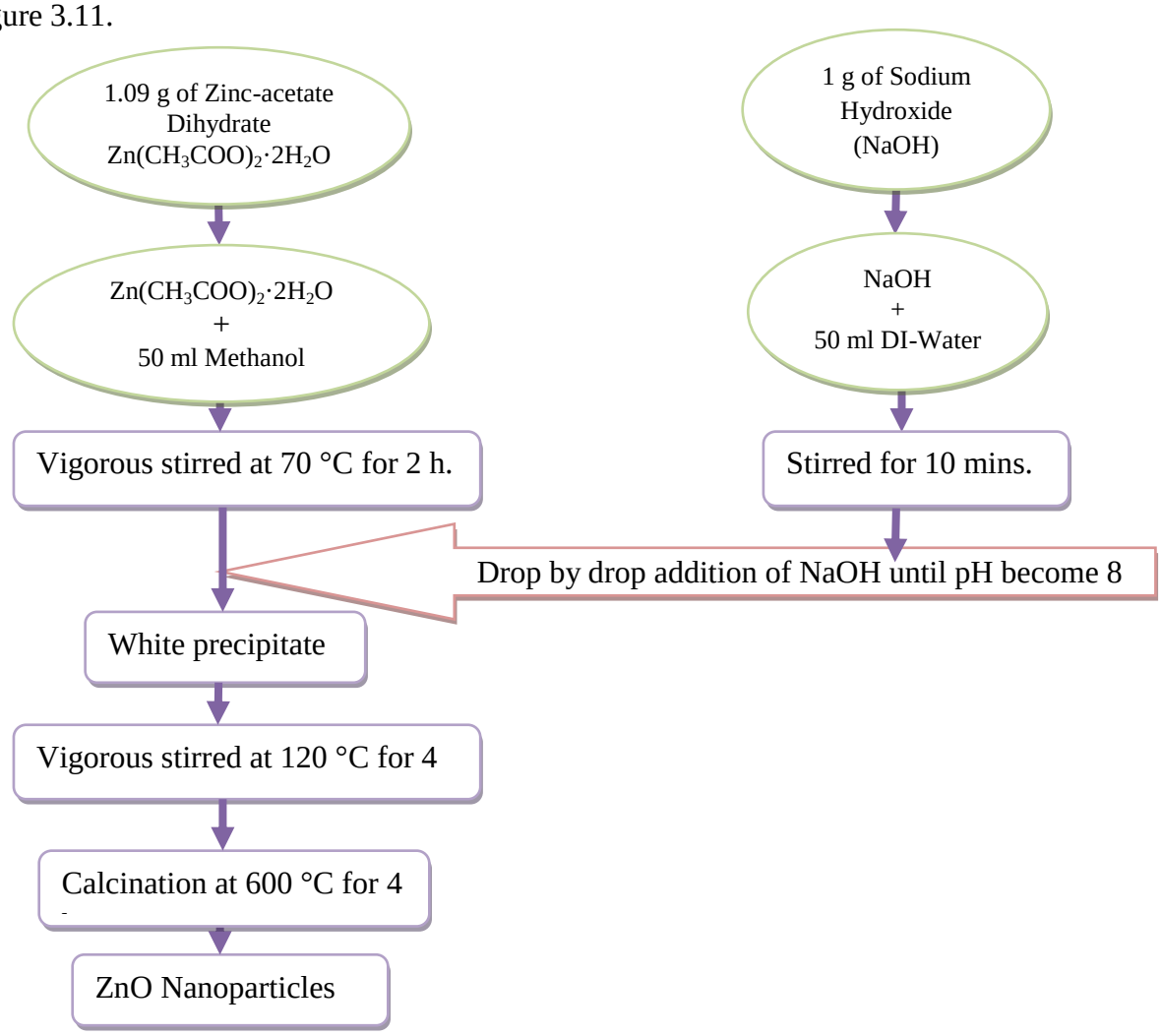

Figure 3.11: Flowchart of the synthesis of ZnO nanoparticles

3.5.2 Artwork Generation

The artwork for thick film devices are generated by conventional processes such as tape strips, drawing, inking or cut-and-peel techniques. Each method has its own advantages and application. The present work uses the coordinato-graph for generating artwork of heater and electrode pattern. The coordinato-graph generates only layout of the designs which are 10x enlarged of original size. In the next step, the patterns are photographically reduced to

the actual size. These images are directly used to prepared mask on the screen. The heater and electrode pattern for printing stages of the discrete sensor is shown in Figure 3.12 (a) & (b) respectively. The dimension of the electrode is mentioned in Table 3.1

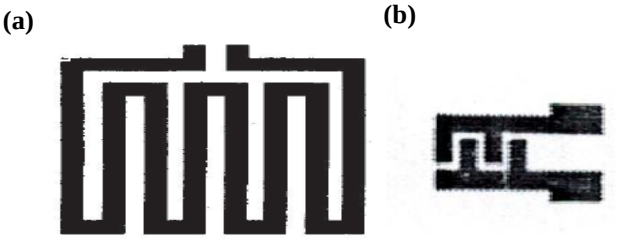

Figure 3.12: Top view of (a) heater and (b) inter-digited gold electrode artwork.

Table 3.1: Geometrical details of the electrode pattern of the sensor.

Parameters	Sensor's dimension (mm)
Length of electrode fingers	1.5
Width of electrode fingers	1
Inter-electrode spacing	0.5

3.5.3 Screen Preparation

Thick film is deposited by screen printing technology in which the electrode and heater paste is printed on the alumina substrate through screen during the printing process. The screen consists of a cast aluminum frame with a finely woven mesh having some important properties such as size, mesh count, tension, orientation, and material. This mesh consists of around 200 strands per inch in a screen and polyester, nylon or stainless steel materials are used for screen meshes. The screen also should be an adequately flexible and elastic so that it makes good contact area over the substrate and could return to its original position after the printing stroke. The artwork generated heater and electrode pattern are transferred to the nylon screen using the photo-sensitive green solution as shown in Figure 3.13 (a) and (b) respectively.

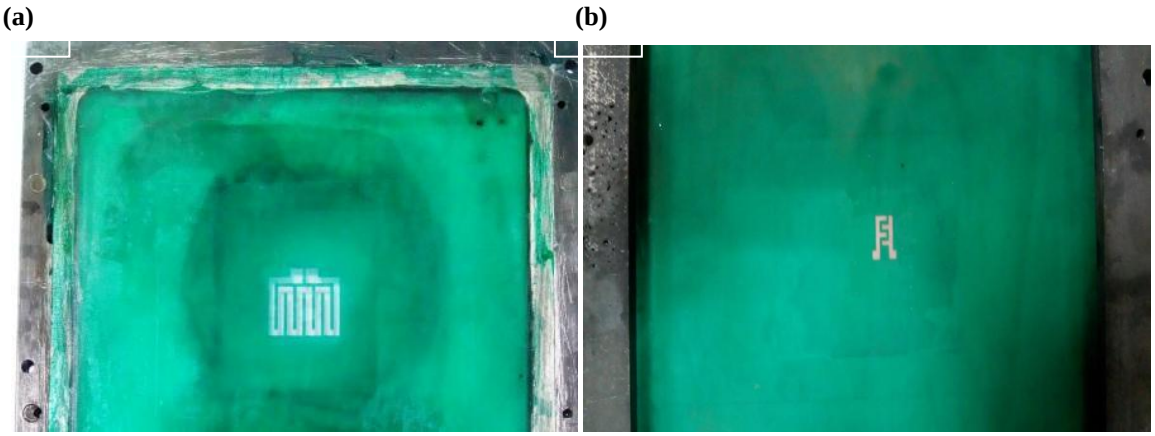

Figure 3.13: Top view of transferred (a) heater (b) electrode pattern in the screen.

3.5.4 Substrate Cleaning

The substrate cleaning is a very important part for any electronic device fabrication. For, thick film deposition techniques, the substrate material should have a very low electrical conductivity, robust and thermally stable at high temperature (~ 1000 °C). Alumina substrate posses all the desired quality and therefore aluminum oxide (96 % Al_2O_3) having 1" x 1" inches dimension has been selected as a substrate material. The cleaning of the alumina substrate is done by ultra-sonication of the substrate using soap solution, acetone, and propanol respectively.

3.5.5. Electrode and Heater Printing

The printing technique is most facile and distinctive one, among all the film deposition techniques. In order to fabricate the ZnO resistor, first the electrode and heater pattern were transferred onto the cleaned alumina substrate surface. The deposition of electrode and heater pattern was done by following steps. In first step — the heater pattern was screen printed using a commercially available platinum conductor paste (8836; Electro Science Lab., USA) with the help squeegee onto an alumina substrate.

In the second step, the printed alumina substrate was kept for drying in the electric oven at temperature of 120 °C for 15 min. Lastly, on the rear side of the alumina substrate,

the interdigitated electrode pattern was printed using a commercially available gold paste (5545; Electro Science Lab., USA) and again dried at the temperature of 120 °C for 15 min.

3.5.6. Firing

Firing is the process in which the printed pattern becomes permanently adhered to the alumina substrate and the film acquires all the electrical properties. The printed platinum and gold pastes are co-fired in the conveyor belt furnace (DEK model -840, Germany (GmbH)) in a set temperature profile (total profile duration 40 min) with a peak temperature zone of 850 °C for 40 min.

3.5.7. Brush-coating for ZnO-sensing film

It is a very facile method in order to form a film. In this method, the paste was prepared by the properly mixing of ~ 0.2 g as-synthesized ZnO nanoparticles (NPs) and methanol (~ 1 ml) solution vigorously. In the next, the prepared paste of ZnO NPs was coated onto the interdigitated gold electrode using painting brush as shown in Figure 3.14(a), subsequently; the film was dried at temperature of 200 °C for 15 min.

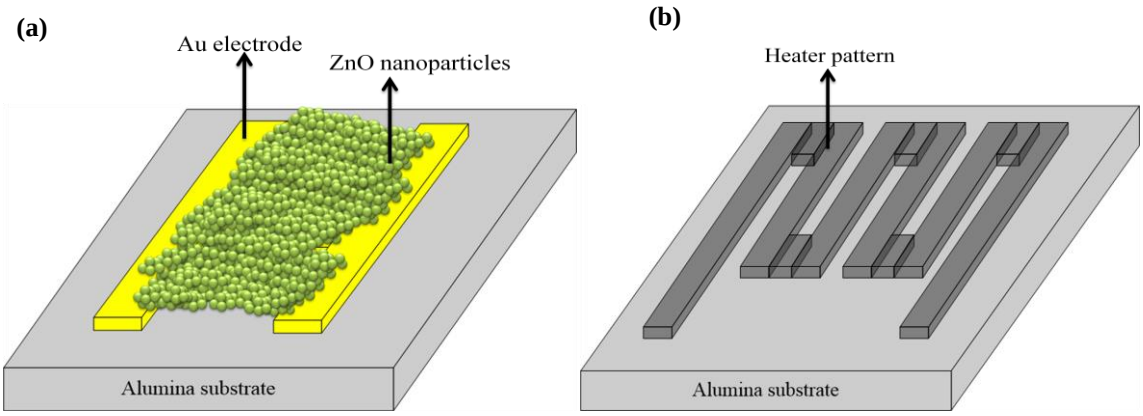

Figure 3.14: Top view of (a) front side of brush coated ZnO nanoparticles on gold-electrode (b) rear side of heater pattern on an alumina substrate.

3.6 Measurement process

The schematic diagram of home-made gas sensing set-up is shown in Figure 3.15. The measurement set-up consists of a gas sensing chamber with two valves dedicated to gas inlet and gas outlet. The fabricated SUT (sensor under test) is kept to the gas sensing chamber (Vol. 3,000 cc). The 6½ digital multimeter is connected to the gold terminals of the resistor via cable. This multimeter displays the precise value of resistance. The heater terminals are connected to the power supply that maintains the temperature of the substrate by varying the power across the heater pattern. The resistance is continuously recorded while injecting a known quantity of gas into the chamber through inlet valve and clearing the chamber by opening the outlet valve. The gas concentration was calculated by the Equation (3.4).

$$\text{Gas Concentration (ppt)} = \frac{\text{Concentration (L)}}{\text{Closed Chamber Volume (L)}} \quad (3.4)$$

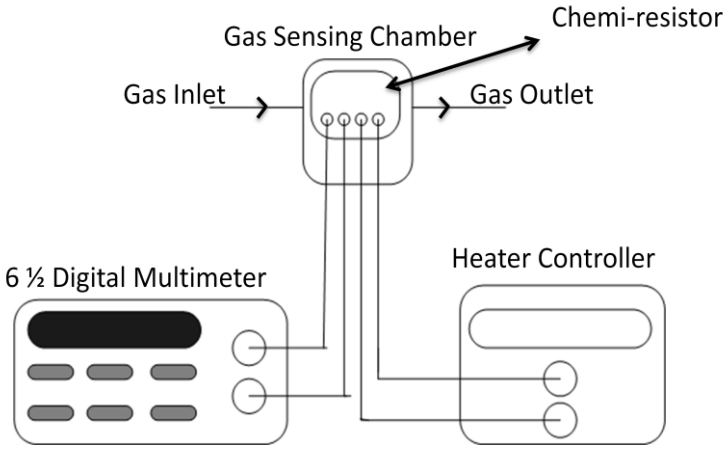

Figure 3.15: Schematic Diagram of Gas Sensing Set-up.

3.7 Result and Discussion

The result and discussion section describe the structural, electrical and gas sensing properties of the fabricated ZnO-resistor.

3.7.1 Structural Results

X-ray diffraction (XRD) pattern of synthesized ZnO nanoparticles (ZnO NPs) is shown in Figure 3.16 (a). The pattern reveals the hexagonal wurtzite structure of ZnO NPs. The crystallite size was found to be ~ 20.12 nm using Scherrer formula $D = 0.89\lambda/(\beta\cos\theta)$, where λ is Cu Kα radiation wavelength (λ = 0.154 nm), β represents the full width at half-maximum (FWHM) and θ is called as diffraction angle (Eriksson *et al.*, 2009; Srivastava, Gusain and Sharma, 2013; Elangovan *et al.*, 2015). In the XRD spectrum, multiple peak intensities of orientation (100), (002), (101), (102), (110), (103), (200), (112) and (201) at 2θ angles 31.79º, 34.42º, 36.26º, 47.55º, 56.62º, 62.9º, 66.4º, 68º, 69.14º respectively reveal that the structure is polycrystalline. The specific 2θ angle and their intensities of the diffraction peaks are confirmed by the powder diffraction standards data (JCPDS No. 36-1451) (Yi *et al.*, 2007). The surface morphology of brush-coated film was analyzed by Atomic Force Microscopy (AFM) in 5 µm scale range as shown in Figure 3.16 (b). This AFM image reveals the average roughness of ~ 107.368 nm and roughness mean square (RMS) of ~ 136.303 nm. Field emission scanning electron microscopy (FE-SEM) is used for exploring and investigating the particles size of the film (Eriksson *et al.*, 2009). Figure 3.16 (c) depicts the ZnO NPs ranging from ~ 25 to ~ 110 nm. Figure 3.16 (d) shows the energy dispersive X-ray spectroscopy (EDS) of ZnO NPs in the range of 0 to 6 KeV (in X-axis) which reveals the only, zinc (Zn) and oxygen (O) elements in the nanoparticles. In EDS, the optical absorption is represented in terms of counts with corresponding energy in the graph and the peaks are due to this absorption.

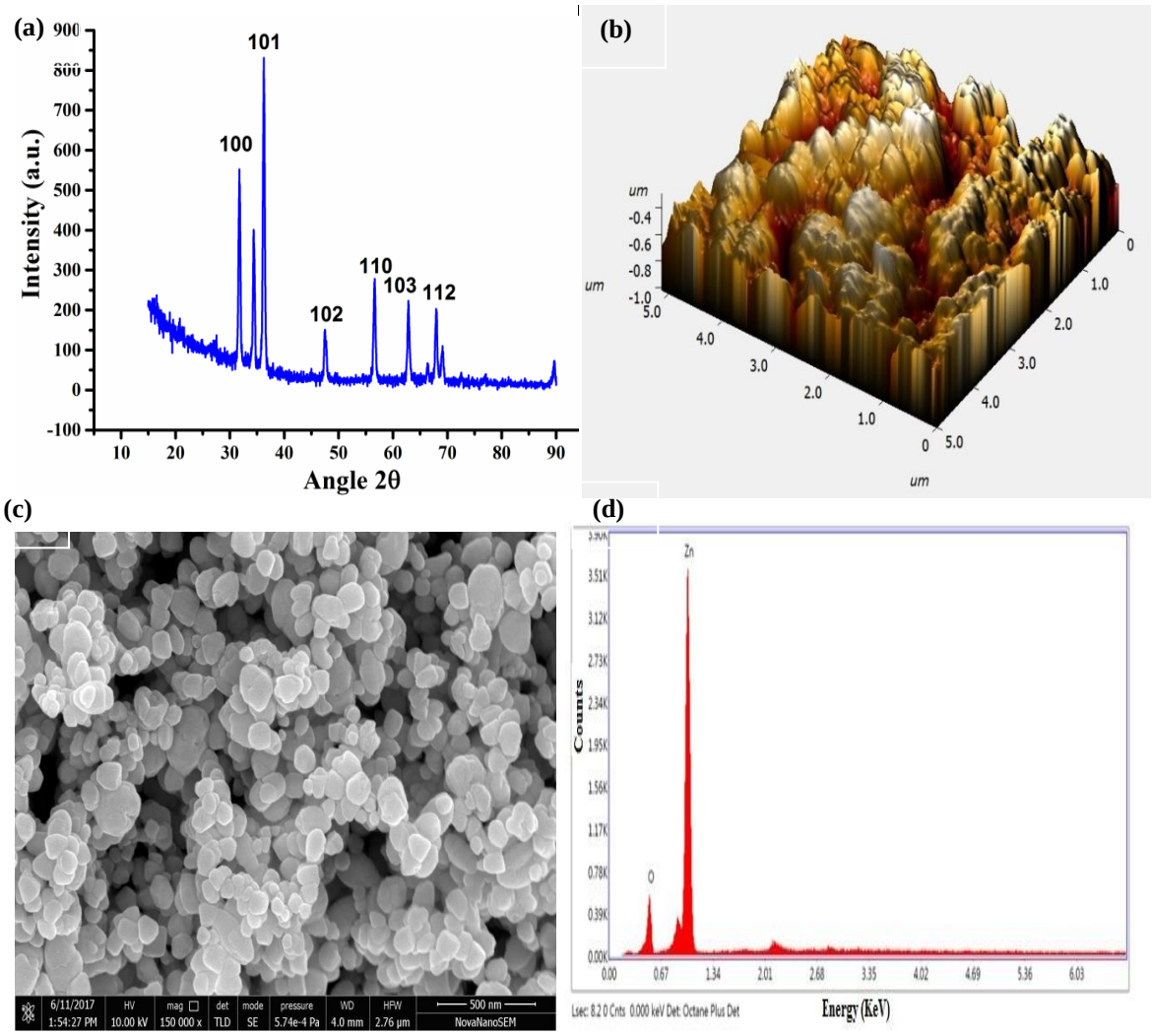

Figure 3.16: Images of (a) XRD (b) AFM (C) FE-SEM and (d) EDS of ZnO nanoparticles.

3.7.2 Gas Sensing Results

Gas sensing measurement has been carried out in the measurement set-up as shown in Figure 3.15. It is well known that semiconductor metal oxide (in this case ZnO) based gas sensor detects the various gases as a change in the charge concentration due to gas adsorption and desorption on the sensor's surface. So, before the gas exposure, the resistance (R_{air}) of ZnO nanoparticles based sensor was stabilized in dry air. Tested gases (NO_2, H_2, CO, Ethanol, propanol) of specific concentration were introduced into the test chamber and changes in the sensor's resistance (R_{gas}) were recorded using multimeter. The sensor's

sensitivity upon the various gases defined by Equation (3.5) (Chougule, Sen and Patil, 2012a, 2012b)

$$S\ (\%) = \frac{\Delta R}{R_{air}} \times 100 \qquad (3.5)$$

Where $\Delta R = \mid R_{air} - R_{gas} \mid$.

The sensitivity of NO_2 gas was measured at 0.1 ppt (parts per thousand) but for the rest of gases (H_2, CO, ethanol, and propanol) the sensitivity was measured at 3.333 ppt concentration in the temperature range 150 to 350 °C. The comparison, amongst all of the gases, has been done by sensitivity (%)/ppt. The sensitivity (%)/ppt was observed for all tested gases in the temperature range from 150 to 350 °C. The NO_2 reports ~ 100 to ~ 942 %/ppt (highest ~ 941.2 %/ppt at 280 °C), ethanol reports ~ 5 to ~20 %/ppt (highest ~ 20.61 %/ppt at 300 °C), H_2 reports ~ 4 to ~11 %/ppt (highest ~ 11.27 %/ppt at 240 °C), propanol reports ~ 3 to ~7 %/ppt (highest ~ 7.09 %/ppt at 280 °C) and CO reports ~ 1 to ~2 %/ppt (highest ~ 2.04 %/ppt at 260 °C) as shown in Figure 3.17 (a). The NO_2 shows ~ 50 times more sensitivity (at around temperature 280 °C) than followed ethanol gas as shown in Figure 3.17 (a). In next step, the sensor was stabilized in the dry air and then continuously exposed to NO_2 gas in the range from 0.1 to 0.234 ppt at operating temperature 280 °C. The resistance transition response upon expose of NO_2 is shown in Figure 3.17 (b). It shows the increase in resistance of the ZnO nanoparticles based film, as increase in exposure of NO_2 gas upon the sensor.

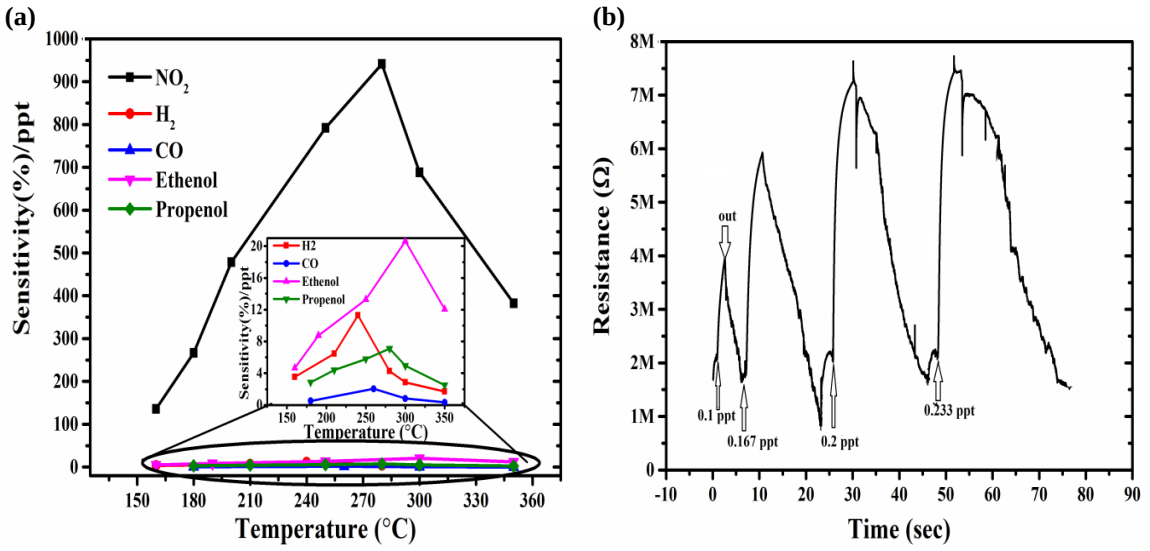

Figure 3.17: (a) As the change in the temperature range from 160 to 350 °C the sensitivity(%)/ppt plot of NO_2, H_2, CO ethanol, propanol. (b) Dynamic resistance of ZnO nanoparticles based resistor upon exposure of 0.1 to 0.234 ppt NO_2 concentration at 280°C.

The sensing mechanism of highly sensitive NO_2 gas can be explained by the change in the electron concentration or resistance of ZnO film upon exposure to the NO_2 gas. The change in resistance is primarily caused by the chemical adsorption and reaction of the oxygen molecules on the surface of the sensing material as shown in Figure 3.18 (a). These chemisorbed oxygen ions act as surface acceptors by trapping electrons from ZnO surface and increases the resistance of the metal oxides as shown in chemical Equation (3.6 to 3.8) (Xia *et al.*, 2008).

$$O_2\,(gas) + e^- \longrightarrow O_2^-\,(ads) \qquad T < 100\ ^\circ C \qquad (3.6)$$

$$O_2^-\,(ads) + e^- \longrightarrow 2O^-\,(ads) \qquad 100^\circ C \leq T \leq 300\ ^\circ C \qquad (3.7)$$

$$O^-\,(ads) + e^- \longrightarrow O^{2-}\,(ads) \qquad T > 300\ ^\circ C \qquad (3.8)$$

NO_2 molecules can not only capture the electrons of the semiconductor due to its higher electrophilic property but also react with the adsorbed oxygen ions as shown in Figure 3.18 (b). The process could be described by chemical Equation (3.9 & 3.10) (Bai *et al.*, 2012)

$$NO_2(gas) + e^- \longrightarrow NO_2^-(ads) \quad (3.9)$$

$$NO_2^-(ads) + 2O^-(ads) + e^- \longrightarrow NO_2(gas) + 2O^{2-}(ads) \quad (3.10)$$

These above cyclic reactions results in a decrease in the electron concentration on the material surface, which lead to the decrease in conductivity or increase in resistivity. In another word, these cyclic reactions of NO_2 on ZnO surface increases the barrier height. It creates barrier for transportation of charge carrier as shown in Figure 3.18 (b), which in turn the increase in ZnO resistance.

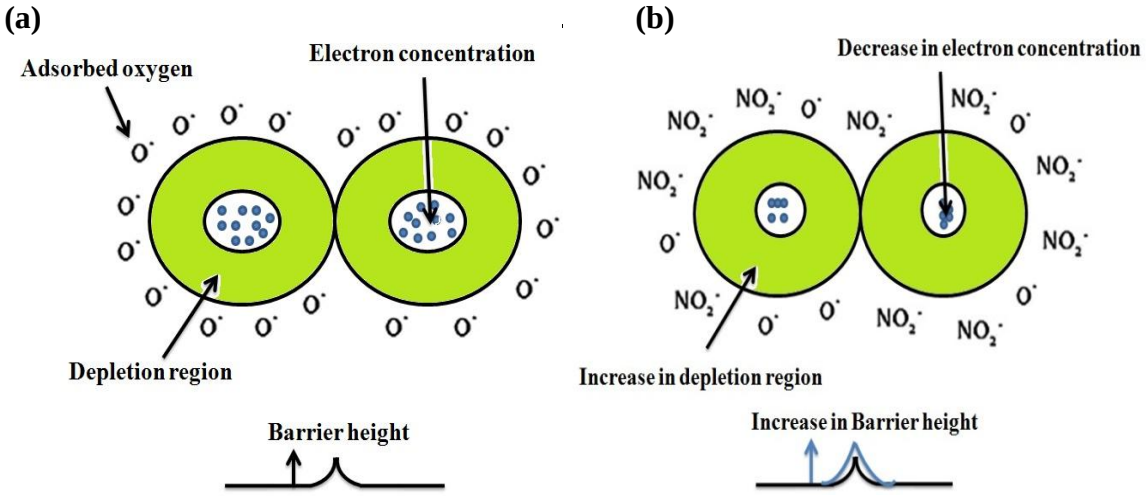

Figure 3.18: (a) Adsorption of oxygen ions on the gains of ZnO before exposure of NO_2 (b) Chemisorption of NO_2 ions after exposing of NO_2 molecules.

The time domain percentage sensitivity of the sensor upon increasing NO_2 exposure (0.1 to 0.234 ppt) is shown in Figure 3.19 (a). It is observed that the sensitivity increases (~ 95 to ~ 275 %) as increase in NO_2 concentration. Figure 3.19 (b) shows the sensitivity in percentage upon exposure of NO_2 concentration from 0.00 to 0.234 ppt. Initially, the

sensitivity increases with increase in NO_2 concentration; most probably due to the linear increase in NO_2^- ions on the ZnO surface which led to a deficiency in the electron. Furthermore, increase in the NO_2 concentration the sensitivity move towards to saturation trend; most probably due to complete filling the adsorption site present on the ZnO nanoparticles surface which not allows to furthermore decreasing in electron concentration.

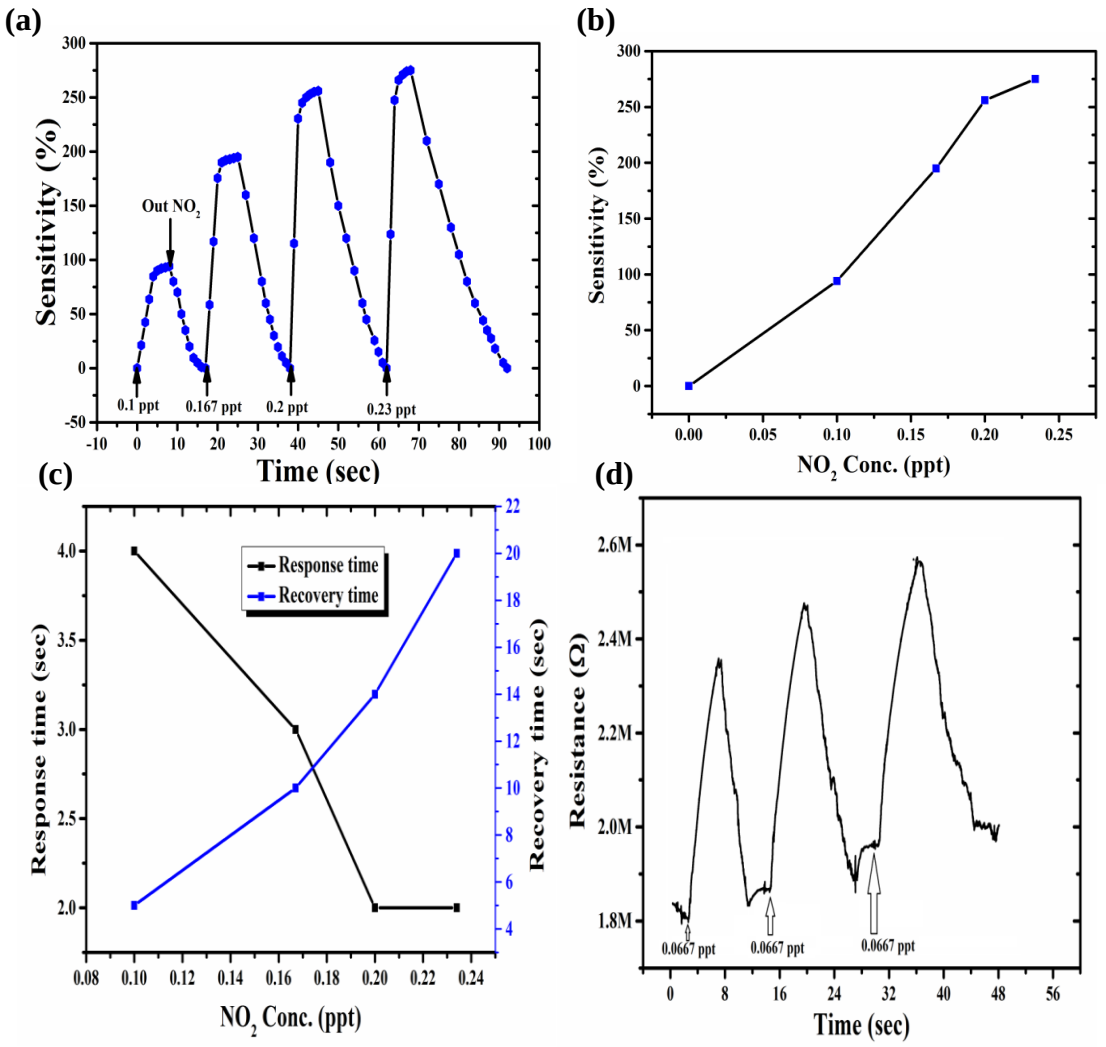

Figure 3.19: (a) The dynamic sensitivity of sensor (b) Increase in sensitivity as increase in NO_2 concentration (c) Change in response and recovery time with increasing NO_2 concentration (d) repeatable sensitivity at 280 °C.

The response and recovery time is an important parameter for characterizing a sensor's performance. The Response time is defined as the time taken by the sensor to attain

90% of the maximum resistance on exposure of NO_2 gas and recovery time as the time to get back 10% of its maximum resistance (Kadhim, Abu Hassan and Abdullah, 2016; Thu *et al.*, 2017a). Figure 3.19 (c) reports the response and recovery time of the sensor upon exposure of NO_2 concentration from 0.1 to 0.23 ppt at 280 °C. It is observed in the Figure 3.19 (c) that the response time is shorter than the recovery time. Response time shows a decreasing trend (4 to 2 s) with increase in NO_2 concentration (0.1 to 0.234 ppt); most probably due higher chemisorption rate at larger concentration of test gas. In contrast to recovery time increases (5 to 20 s) as increase in NO_2 concentration (0.1 to 0.234 ppt) at operating temperature 280 °C; most probably due to lower desorbing rate of NO_2. The sensor also shows the very good repeatable sensitivity as shown in Figure 3.19 (d). This repeatable sensitivity shows the reliable performance of the sensor. Figure 3.19 (d) also shows the slight change in sensitivity around ~ 35 % upon exposure to three consecutive 0.0667 ppt NO_2 concentration at an operating temperature of 280 °C.

3.8 Conclusion

The chapter 3 discusses the available facility for resistive based sensor fabrication and characterization such as manual thick film printer, oven, conveyor belt furnace and self-developed measurement set-up. This chapter also elaborates the material characterization tools such as SEM, XRD, AFM, and EDS. In this chapter, the successful fabrication of highly selective, resistor type, ZnO nanoparticles based NO_2 sensor using sol-gel brush coated technique has been discussed. The film was characterized by FE-SEM, XRD, AFM, and EDS which confirms the ZnO material having a particle size of ~ 25 to ~ 110 nm and roughness of ~ 136.303 nm. The gas sensing properties of the sensor have been studied for various gases such as NO_2, H_2, CO, ethanol, and propanol in the temperature range from 150 to 350 °C. Among all these tested gases, NO_2 reported the highest sensitivity ~ 945 %/ ppt at operating

temperature of 280 °C. The obtained results have been explained by the surface and subsurface adsorption of NO_2 molecules at available trap sites (oxygen ions) on the nanoparticles (ZnO) surface. Fast response and recovery time with excellence repeatability have also been observed. The increased NO_2 concentration (0.1 to 0.234 ppt) affects the response and recovery times; the response time decreases from 4 to 2s with an increase in recovery time from 5 to 20 s.

References

Bai, S. *et al.* "Gas sensing properties of quantum-sized ZnO nanoparticles for NO2", *IEEE Sensors Journal*, 2012, vol. 12, no. 5, pp. 1234–1238.

Bari, A. R. *et al.* "Effect of solvents on the particle morphology of nanostructured ZnO", *Indian Journal of Pure & Applied Physics*, 2009, vol. 47, pp. 24–27.

Chougule, M. A., Sen, S. and Patil, V. B. "Development of nanostructured polypyrrole (PPy) thin film sensor for NO2 detection", *Sensors and Transducers*, 2012, vol. 9, no. 5, pp. 482–490.

Chougule, M. A., Sen, S. and Patil, V. B. "Fabrication of nanostructured ZnO thin film sensor for NO2 monitoring", *Ceramics International*, 2012, vol. 38, pp. 2685–2692.

Connolly, J. R. "'Introduction to X-ray Powder Diffractometry'", in. Springer, 1996, , pp. 1–9.

Elangovan, S. V. *et al.* "Synthesis and characterization of sodium doped ZnO nanocrystals and its application to photocatalysis", *Superlattices and Microstructures*, 2015, vol. 85, pp. 901–907.

Eriksson, J. *et al.* "ZnO nanoparticles or ZnO films: A comparison of the gas sensing capabilities", *Sensors and Actuators B*, 2009, vol. 137, pp. 94–102.

Gnanamoorthy, P., Karthikeyan, V. and Prabu, V. A. "Field emission scanning electron microscopy (FESEM) characterisation of the porous silica nanoparticulate structure of marine diatoms", *Journal of Porous Materials*, 2014, vol. 21, no. 2, pp. 225–233.

Harrers, D. *Scanning tunneling microscope vs . scanning electron microscope*. Test and measurement tips, 2016,

Hasnidawani, J. N. *et al.* "Synthesis of ZnO Nanostructures Using Sol-Gel Method", *Procedia Chemistry*, 2016, vol. 19, no. 1, pp. 211–216.

Jena, B. P. et al. "'Instreuments for structural, Optical, Electrical Characterizations'", in. Sodh ganga, 2014, , pp. 65–92.

Kadhim, I. H., Abu Hassan, H. and Abdullah, Q. N. "Hydrogen gas sensor based on nanocrystalline SnO2 Thin Film grown on bare Si substrates", *Nano-Micro Letters*, 2016, vol. 8, no. 1, pp. 20–28.

Kamarulzaman, N. and Jaafar, M. H. "'Synthesis and Stoichiometric Analysis of a Li-Ion Battery Cathode Material'", in. Centre For Foundation Study In Sciences, University of Malaya, Kuala Lumpur, 2003, , pp. 247–262.

Mao, S., Lu, G. and Chen, J. "Nanocarbon-based gas sensors: Progress and challenges", *Journal of Materials Chemistry A*, 2014, vol. 2, no. 16, pp. 5573–5579.

Navale, S. T. *et al.* "Room temperature NO2sensing properties of polythiophene films", *Synthetic Metals*, 2014, vol. 195, pp. 228–233.

Van Quang, V. *et al.* "Outstanding gas-sensing performance of graphene/SnO2 nanowire Schottky junctions", *Applied Physics Letters*, 2014, vol. 105, no. 1, p. 13107.

Quate, G. B. and C. F. "Atomic Force Microscope", *Physical review letters*, 1986, vol. 56, no. 9, pp. 930–933.

Rai, P. *et al.* "The role of gold catalyst on the sensing behavior of ZnO nanorods for CO and NO2 gases", *Sensors and Actuators, B: Chemical*, 2012, vol. 165, no. 1, pp. 133–142.

Rai, P. and Yu, Y. "Citrate-assisted hydrothermal synthesis of single crystalline ZnO nanoparticles for gas sensor application", *Sensors and Actuators B: Chemical*, 2012, vol. 173, no. 2, pp. 58–65.

Sadek, A. Z. *et al.* "Characterization of ZnO nanobelt-based gas sensor for H2, NO2, and hydrocarbon sensing", *IEEE Sensors Journal*, 2007, vol. 7, no. 6, pp. 919–924.

Shim, Y. *et al.* "Chemical Highly sensitive and selective H2 and NO2 gas sensors based on surface-decorated WO3 nanoigloos", *Sensors & Actuators: B. Chemical*, 2014, vol. 198, no. 2, pp. 294–301.

Srivastava, V., Gusain, D. and Sharma, Y. C. "Synthesis, characterization and application of zinc oxide nanoparticles (n-ZnO)", *Ceramics International*, 2013, vol. 39, no. 8, pp. 9803–9808.

Swaminathan, P. "'Lecture 3: X-ray diffraction and methods'", in. U D Physics, 2013, ,

pp. 1–19.

Thu, D. T. *et al.* "Schottky contacts of (Au, Pt)/nanotube-titanates for fast response to NO2 gas at room temperature", *Sensors and Actuators B: Chemical*, 2017, vol. 244, pp. 941–948.

Thu, D. T. *et al.* "Schottky contacts of (Au, Pt)/nanotube-titanates for fast response to NO2gas at room temperature", *Sensors and Actuators, B: Chemical*, 2017, vol. 244, pp. 941–948.

Urasinska-Wojcik, B. *et al.* "Ultrasensitive WO3gas sensors for NO2 detection in air and low oxygen environment", *Sensors and Actuators, B: Chemical*, 2017, vol. 239, pp. 1051–1059.

Wang, J. X. *et al.* "Hydrothermally grown oriented ZnO nanorod arrays for gas sensing applications", *Nanotechnology*, 2006, vol. 17, pp. 4995–4998.

Xia, H. *et al.* "Chemical Au-doped WO3 based sensor for NO2 detection at low operating temperature", *Sensors and Actuators B*, 2008, vol. 134, no. 2, pp. 133–139.

Yi, S.-H. *et al.* "Low-temperature growth of ZnO nanorods by chemical bath deposition", *Journal of Colloid and Interface Science*, 2007, vol. 313, pp. 705–710.

[IR5] http://en.wikipedia.org/wiki/Bragg’s law.